

The acoustic resonance of rectangular and cylindrical cavities

A. Rona *,¹

Department of Engineering, University of Leicester, LE1 7RH, UK

ABSTRACT

An investigation is conducted on the acoustic resonance that develops in rectangular and cylindrical cavities with rigid walls. An analytical model for the small amplitude acoustic perturbations inside an enclosure with rigid walls is developed from classical linerized acoustics. The method is first applied to a rectangular geometry and the normalized mode shapes and frequencies of the first six standing wave modes are given. The results are used to diagnose whether coupling is likely to occur between the first two Rossiter modes and the acoustic standing waves, which may lead to a reinforcement of the flow instability. At the selected test conditions, the method indicates that the second Rossiter mode can couple with the first longitudinal acoustic mode. The acoustic resonant mode predictions for a cylindrical cavity of length to depth ratios 0.71 and 2.5, tested at near-incompressible speeds, suggest that the acoustic resonant modes and the main fluid dynamic instability in the enclosure are sufficiently apart in frequency not to strongly interact with one another. The parametrized analytical solutions developed in this study enable the aero-acoustic engineer to diagnose whether coupling between a given fluid dynamic instability and acoustic resonance is likely to affect a rectangular or cylindrical cavity component.

Key words: Computational fluid dynamics; acoustic resonance; cavity flow
PACS: 47.11.+j, 43.28.+h, 47.85.Gj.

*Corresponding Author. Address: Department of Engineering, University of Leicester, Leicester LE1 7RH, Tel. +44-116-252 2510, Fax: +44-116-252 2525.

Email address: ar45@le.ac.uk (A. Rona).

URL: <http://www.le.ac.uk/eg/ar45> (A. Rona).

¹Lecturer.

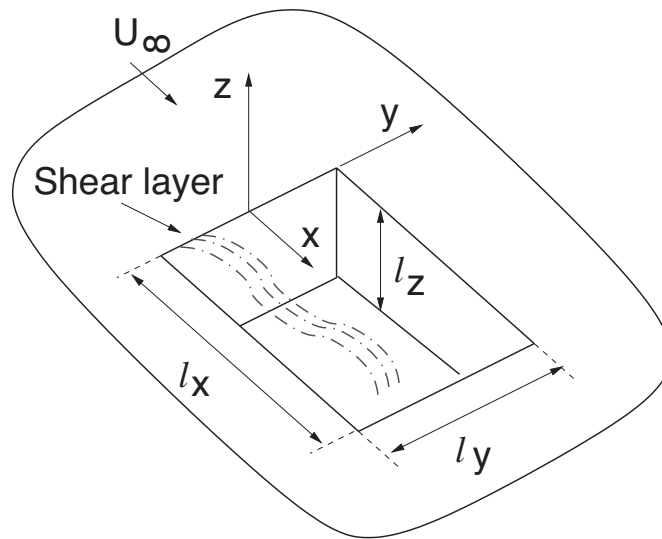


Figure 1. Rectangular cavity.

1. INTRODUCTION

The grazing flow past a surface cut-out can develop instabilities that adversely affect the aerodynamic performance of airframe, automotive, and railway components. Such instabilities can be either fluid dynamic, hydroelastic or flow-resonant, depending on whether aeroelastic or acoustic effects contribute to the flow unsteadiness.

The flow past the surface cut-out, or cavity, separates at the upstream edge, forming a shear layer, as shown in figure 1. Provided the cavity streamwise length to depth ratio (L/D) is low, typically $L/D \leq 6$, the shear layer spans across the cavity opening and reattaches on the downstream wall, forming an ‘open’ cavity flow [1]. The known fluid dynamic instability processes for open cavities, as reviewed by Rowley & Williams [2], are the Rossiter mechanism, whereby a downstream travelling shear-layer convective instability couples with an upstream feed-back wave inside the cavity, and the wake mode, which is a purely hydrodynamic instability [2] with global instability type features [3].

For a given inflow condition and geometry, a cavity fluid dynamic instability can manifest itself as limit cycle modes spanning a specific frequency range. The presence of acoustic or aeroelastic resonant modes in an open cavity over the same frequency range can play an important role in mode selection [2] and in phase-locking the feed-back process.

This paper presents an analytical method to determine the first six acoustic modes of a rectangular and of a cylindrical enclosure, so that the fluid dynamic practitioner can test whether, at a given operating condition, the instability is susceptible to acoustic resonance driven enhancement.

2. ANALYTICAL METHOD

The analytical method follows closely the conventional approach to determine the room modes in building acoustics. The acoustic pressure fluctuation inside an enclosure at International Standard Atmosphere ground conditions is small compared to the atmospheric pressure, so it can be regarded as an isentropic perturbation of the cavity time-averaged internal pressure. Inside the enclosure, the acoustic pressure fluctuation at location \mathbf{x} and time t is governed by the wave equation

$$\left(\frac{1}{a_c^2} \frac{\partial^2}{\partial t^2} - \nabla^2 \right) p(\mathbf{x}, t) = 0 \quad (1)$$

where a is the speed of sound and subscript c denotes the flow state inside the enclosure [4]. For a statistically stationary flow, the pressure perturbation can be decomposed into a summation of orthogonal Fourier components

$$p(\mathbf{x}, t) = \sum_{h=-\infty}^{\infty} p_h(\mathbf{x}) \cos(\omega_h t - \phi_h) \quad (2)$$

where ω_h is the h^{th} Fourier component angular frequency and ϕ_h is its phase angle at $t = 0$. Substituting Eq. (2) in Eq. (1) and imposing that each Fourier component satisfies Eq. (1) independently at all times gives the Helmholtz equation

$$\left(\nabla^2 + k_h^2 \right) p_h(\mathbf{x}) = 0 \quad (3)$$

where $k_h = \omega_h/a_c$ is the wavenumber of the h^{th} Fourier component.

Equation (3) is a second-order partial differential equation, therefore its solution requires two independent boundary conditions per spatial dimension. For an enclosure with rigid solid walls, the wall-normal flow velocity is zero. Therefore, by the conservation of momentum for inviscid flows,

$$\nabla p_h(\mathbf{x}) \cdot \mathbf{n} = 0 \quad (4)$$

at the rigid walls, where \mathbf{n} is the inward wall-normal unit vector.

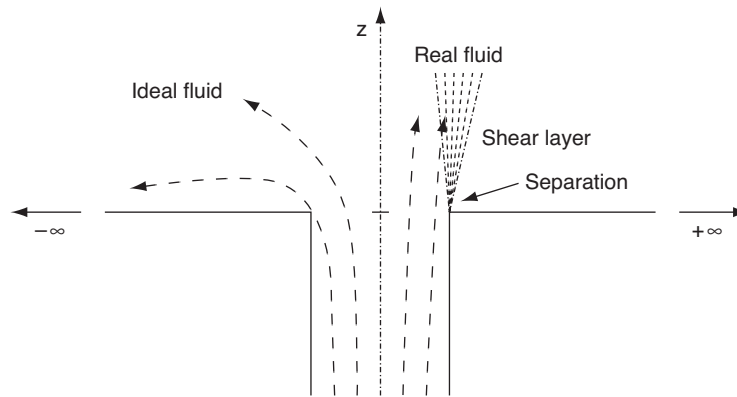


Figure 2. Abrupt flow expansion from a rectangular channel.

At the cavity open end, a simple acoustic reflecting boundary condition is imposed. This condition is derived from classical duct acoustics, by considering an ideal abrupt expansion, as shown in figure 2. Consider the normal (vertical) flow across the cavity opening induced by the flow-normal (vertical) acoustic velocity just below the $z = 0$ plane. A real flow would separate at the cavity mouth, forming a jet that dissipates the kinetic energy of the acoustic velocity by viscous stresses in the jet shear layer. This dissipative mechanism results in a damped oscillation and this process is used, for instance, to design tuned acoustic dampers in a jet engine tail-cone. As this study seeks to identify the cavity undamped natural modes, a flow condition is sought at the $z = 0$ plane that prevents the onset of this dissipative mechanism. A simple condition that satisfies this requirement is to impose the flow-normal acoustic velocity at the cavity open end to be zero. At this condition, applying the conservation of momentum for inviscid flows in the flow-normal direction gives

$$\frac{\partial}{\partial z} p_h(x, y, 0) = 0 \quad (5)$$

The boundary condition of Eq. (5) is a strong hypothesis in the analytical model, as cavity flows typically feature flow-normal velocity fluctuations across the opening, driven by the unsteady shear layer, as sketched in figure 1. Such velocity fluctuations can be split between a viscous hydrodynamic component, associated to the unsteady hydrodynamic pressure and vorticity in the shear layer, and an inviscid acoustic perturbation, associated to the cavity acoustic field [5–7]. At low Mach numbers, the hydrodynamic component is dominant and the unsteady flow in the cavity can be successfully modelled by

an incompressible viscous formulation that neglects the inviscid acoustic perturbation [6,7]. At these conditions, setting the flow-normal acoustic velocity across the opening as zero amounts to neglecting one out of three components of the local acoustic velocity fluctuation, which is a small perturbation of the local flow velocity. Therefore the boundary condition of Eq. (5) is compatible with the known physics of low Mach number cavity flows. A more sophisticated boundary condition for the cavity open end is available in the literature [4], derived by considering the dynamic equilibrium of a two-dimensional vortex sheet that models the open cavity shear layer. The use of such a condition would be a useful extension to the present work.

For an arbitrary shaped flat-top open cavity geometry, Eq. (3) can be solved together with the boundary conditions of Eqs. (4) and (5) to determine the acoustic pressure spatial distribution inside the enclosure.

3. MODELLING THE NATURAL ACOUSTIC MODES OF A RECTANGULAR CAVITY

3.1. The Eigen-frequencies

In the Cartesian reference system of figure 1, Eq. (3) becomes

$$\left(\frac{\partial^2}{\partial x^2} + \frac{\partial^2}{\partial y^2} + \frac{\partial^2}{\partial z^2} + k_h^2 \right) p_h(x, y, z) = 0 \quad (6)$$

Similarly, the boundary conditions of Eqs. (4) and (5) become

$$\frac{\partial}{\partial x} p_h(0, y, z) = 0 \quad (7)$$

$$\frac{\partial}{\partial x} p_h(l_x, y, z) = 0 \quad (8)$$

$$\frac{\partial}{\partial y} p_h \left(x, \pm \frac{l_y}{2}, z \right) = 0 \quad (9)$$

$$\frac{\partial}{\partial z} p_h(x, y, -l_z) = 0 \quad (10)$$

$$\frac{\partial}{\partial z} p_h(x, y, 0) = 0 \quad (11)$$

Equation (6) is solved by the separation of variables approach. Let $p_h(x, y, z) = p_x(x) p_y(y) p_z(z)$. Substituting for p_h in Eq. (6) and dividing throughout by $p_x p_y p_z$ gives

$$\frac{1}{p_x} \frac{\partial^2}{\partial x^2} p_x + \frac{1}{p_z} \frac{\partial^2}{\partial z^2} p_z + k_h^2 = -\frac{1}{p_y} \frac{\partial^2}{\partial y^2} p_y \quad (12)$$

The left hand side of Eq. (12) is independent from y while the right hand side is independent from x and z . Therefore, the two sides of the equation must match by a constant η^2 , independent from x , y and z . This decouples the system into

$$\frac{1}{p_x} \frac{\partial^2}{\partial x^2} p_x + k_h^2 - \eta^2 = -\frac{1}{p_z} \frac{\partial^2}{\partial z^2} p_z \quad (13)$$

$$\left(\frac{\partial^2}{\partial y^2} + \eta^2 \right) p_y = 0 \quad (14)$$

Applying recursively the same argument to Eq. (13) by the use of a second constant ζ^2 gives

$$\left(\frac{\partial^2}{\partial x^2} + k_h^2 - \eta^2 - \zeta^2 \right) p_x = 0 \quad (15)$$

$$\left(\frac{\partial^2}{\partial y^2} + \eta^2 \right) p_y = 0 \quad (16)$$

$$\left(\frac{\partial^2}{\partial z^2} + \zeta^2 \right) p_z = 0 \quad (17)$$

The general solution of Eq. (17) is $p_z = A_z \cos(\zeta z - \alpha_\zeta)$, where A_z is the amplitude of the pressure fluctuation, independent from z , and α_ζ a phase angle to be evaluated using the boundary condition of Eq. (11). Substituting $p_z = A_z \cos(\zeta z - \alpha_\zeta)$ in Eq. (11) gives $-A_z \zeta \sin(-\alpha_\zeta) = 0$, which has roots $\zeta = 0$, implying a uniform pressure in z , and $-\alpha_\zeta = \pm n\pi$, with n integer. Therefore, under the boundary condition of Eq. (11), Eq. (17) reduces to $p_z = A_z \cos(\zeta z \mp n\pi)$. Substituting this in Eq. (10) gives $-A_z \zeta \sin(-\zeta l_z \mp n\pi) = 0$, which has the roots $\zeta = \pm n\pi/l_z$, where $n \geq 0$ is integer. Therefore

$$p_z = A_z \cos(n\pi z / l_z) \quad (18)$$

satisfies Eq. (17) and the boundary conditions of Eqs. (10) and (11).

Analogously, Eq. (16) has the general solution $p_y = A_y \cos(\eta y - \alpha_\eta)$. By substituting this in Eq. (9), $\alpha_\eta = \mp m\pi/2$ and $\eta = \pm m\pi/l_y$, where $m \geq 0$ is integer. This gives

$$p_y = A_y \cos(m\pi y/l_y - m\pi/2) \quad (19)$$

that satisfies Eq. (16) with the boundary conditions of Eq. (9).

Let $\xi^2 = k_h^2 - \eta^2 - \zeta^2$. Substituting for ξ^2 in Eq. (15), Eq. (15) takes the same form of Eqs. (16) and (17) and has the general solution $p_x = A_x \cos(\xi x - \alpha_\xi)$. Substituting this in Eqs. (7) and (8) gives $\alpha_\xi = 0$ and $\xi = \pm l\pi/l_x$, where $l \geq 0$ is integer. Therefore,

$$p_x = A_x \cos(l\pi x/l_x) \quad (20)$$

is a solution of Eq. (15) with the boundary conditions of Eqs. (7) and (8).

From the definition of ξ , the cavity natural mode wavenumbers are

$$k_{l,m,n}^2 = \xi^2 + \eta^2 + \zeta^2 = \left(\frac{l\pi}{l_x}\right)^2 + \left(\frac{m\pi}{l_y}\right)^2 + \left(\frac{n\pi}{l_z}\right)^2 \quad (21)$$

and from $\omega_{l,m,n} = a_c k_{l,m,n}$, the cavity acoustic eigen-frequencies $f_{l,m,n} = \omega_{l,m,n}/(2\pi)$ are

$$f_{l,m,n} = a_c \left[\left(\frac{l}{2l_x}\right)^2 + \left(\frac{m}{2l_y}\right)^2 + \left(\frac{n}{2l_z}\right)^2 \right]^{1/2} \quad (22)$$

where l , m and n are arbitrary integers ≥ 0 .

3.2. The Eigenvectors

The acoustic pressure distribution at the cavity natural frequencies $f_{l,m,n}$ is obtained from combining Eqs. (18), (19) and (20) by $p_h(x, y, z) = p_x(x) p_y(y) p_z(z)$. Let $A_{l,m,n} = A_x A_y A_z$, then

$$p_{l,m,n}(x, y, z) = A_{l,m,n} \cos(\pi l x/l_x) \cos(\pi m y/l_y - m\pi/2) \cos(\pi n z/l_z) \quad (23)$$

Figure 3 shows the first six acoustic natural modes of a rectangular cavity of length to depth ratio $L/D = 2$ and length to width ratio $L/W = 1$. This geometry was investigated numerically by Bissessur et al. [8] at a free-stream Mach number $M_\infty = 0.6$. The constant amplitude planes $A_{l,m,n} = -0.5, 0$ and 0.5 are shown in figure 3. The natural modes are shown of unit amplitude and all lengths are normalized by the cavity length L . The sequence of figures 3(a)-3(f) shows a standing wave pattern with nodes and anti-nodes, with the number of nodal planes increasing with increasing mode number. The time-dependent acoustic pressure fluctuation inside the enclosure due to acoustic resonance is

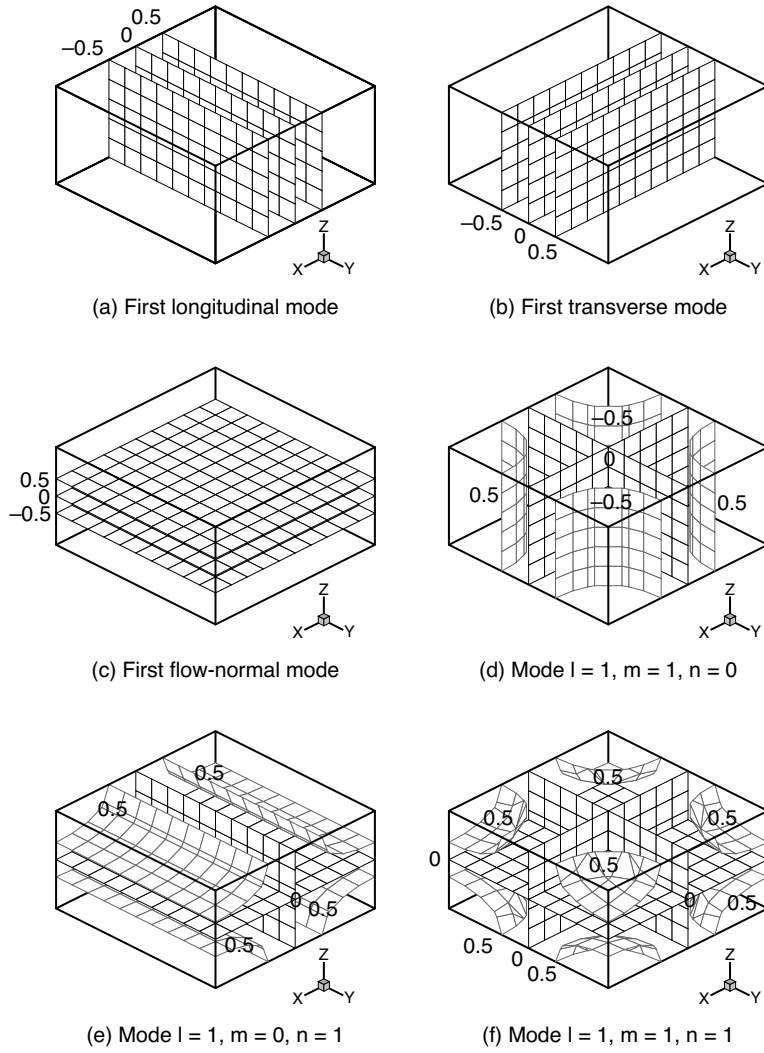


Figure 3. Pressure eigenmodes in a rectangular cavity with rigid walls.

obtained from the linear combination of all the natural modes in the cavity, according to Eq. (2). As the cavity natural modes are orthogonal, then

$$p(x, y, z, t) = \sum_{l=0}^{\infty} \sum_{m=0}^{\infty} \sum_{n=0}^{\infty} p_{l,m,n}(x, y, z) \cos(2\pi f_{l,m,n}t - \phi_{l,m,n}) \quad (24)$$

where $\phi_{l,m,n}$ is the phase reference angle of each mode at time $t = 0$.

3.3. Rectangular Cavity Instability Reinforcement by Acoustic Resonance

Equation (22) can be used to diagnose whether, for a given cavity geometry and inflow Mach number, an enclosure is susceptible to acoustic resonance. Consider an enclosure of streamwise length $l_x = L$, width $l_y = W$ and depth $l_z = D$. Multiplying both sides of Eq. (22) by L/U_∞ , with U_∞ being the free-stream velocity of the external flow approaching the cavity, gives the Strouhal numbers of the cavity acoustic modes

$$Str_{l,m,n} = \frac{f_{l,m,n}L}{U_\infty} = \frac{\left(1 + \frac{\gamma-1}{2}M_\infty^2\right)^{1/2}}{M_\infty} \left[\left(\frac{l}{2}\right)^2 + \left(\frac{m}{2}\frac{L}{W}\right)^2 + \left(\frac{n}{2}\frac{L}{D}\right)^2 \right]^{1/2} \quad (25)$$

where γ is the ratio of the specific heats, C_p/C_v .

Open cavities that feature a shear layer driven instability, commonly referred to as a Rossiter instability, do so at a Strouhal number that can be predicted by the Rossiter equation, modified by Heller & Bliss [9], which is

$$Str_h = \frac{h + \alpha}{\frac{M_\infty}{\left(1 + \frac{\gamma-1}{2}M_\infty^2\right)^{1/2}} + \frac{1}{k_c}} \quad (26)$$

In Eq. (26), h is the Rossiter mode number, which is a positive integer, α is a phase delay in the cavity upstream pressure feed-back, and k_c is the average phase speed of shear-layer convective instabilities across the cavity opening, normalized by U_∞ . Typical values for α and k_c are 0.25 [10] and 0.57 [10].

The necessary condition for a Rossiter mode to be reinforced by the cavity acoustic resonance is that the Strouhal number of a cavity acoustic resonance mode matches one component of the harmonic series of any Rossiter mode, that is $Str_{l,m,n} = oStr_h$, where o is an arbitrary integer. Figure 4 shows the acoustic and fluid dynamic Strouhal numbers of the $L/D = 2$, $L/W = 1$ rectangular geometry studied by Bissessur et al. [8] at $M_\infty = 0.6$. The lines show the Strouhal numbers of the Rossiter modes predicted by the time-resolved numerical method of Bissessur et al. [8]. The dots show the Strouhal numbers of the first 15 acoustic modes from Eq. (25). The latter are plotted versus the number of nodal planes for each mode, which is given by $l + m + n$ and is a measure of the acoustic mode shape complexity. The predictions by Bissessur et al. were obtained on a cluster of 36 Intel Pentium 4 processors, running an in-house CFD code written in Fortran 90 with MPI parallelizing directives [8].

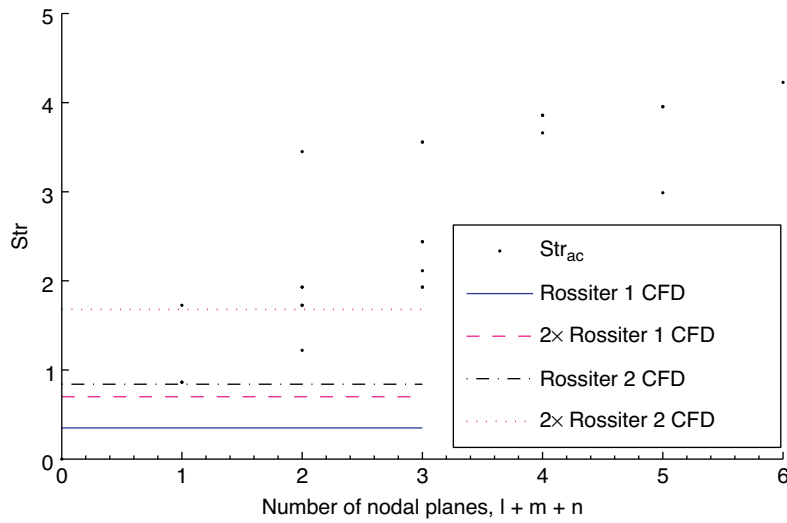


Figure 4. Fluid dynamic and acoustic Strouhal numbers of a $L/D = 2$, $L/W = 1$, Mach 0.6 rectangular cavity flow.

The acoustic Strouhal numbers were obtained by coding Eq. (25) in Matlab 7.0.4. The Matlab script was run on a desktop computer with a 3 GHz Intel Pentium 4 processor and 1 GB of RAM.

Figure 4 shows that only the low acoustic mode numbers have Strouhal numbers close to the Rossiter 1 and 2 modes, which were documented by Bissessur et al. [8] as being the most energetic fluid dynamic modes in the predicted pressure spectra. Specifically, the second Rossiter mode Strouhal number as predicted by Computational Fluid Dynamics (CFD) is within 3% of the Strouhal number of the first longitudinal acoustic mode, $(l, m, n) = (1, 0, 0)$. Similarly, the Strouhal number of the second Rossiter mode second harmonic is also within 3% of the Strouhal number of the second longitudinal acoustic mode, $(l, m, n) = (2, 0, 0)$.

Combining Eq. (25) and Eq. (26), the inflow Mach number at which the fluid dynamic and acoustic Strouhal numbers match is determined. Figure 5 shows the normalized difference in Strouhal numbers, $1 - \sigma S tr_h / S tr_{l,m,n}$, over the Mach number range $0 < M_\infty \leq 1$. The intercepts of $f(M_\infty) = 1 - \sigma S tr_h / S tr_{l,m,n}$ with the abscissa define the Mach numbers at which the Strouhal numbers match, allowing the acoustic reinforcement of a Rossiter mode. $f(M_\infty)$ is shown in figure 5 for the manifold $(1 \leq h \leq 2, 1 \leq l \leq 2, m = 0, n = 0, 1 \leq \sigma \leq 2)$ that is shown in figure 4 as having acoustic and fluid dynamic Strouhal numbers close to each other. The continuous blue curve shows the normalized difference

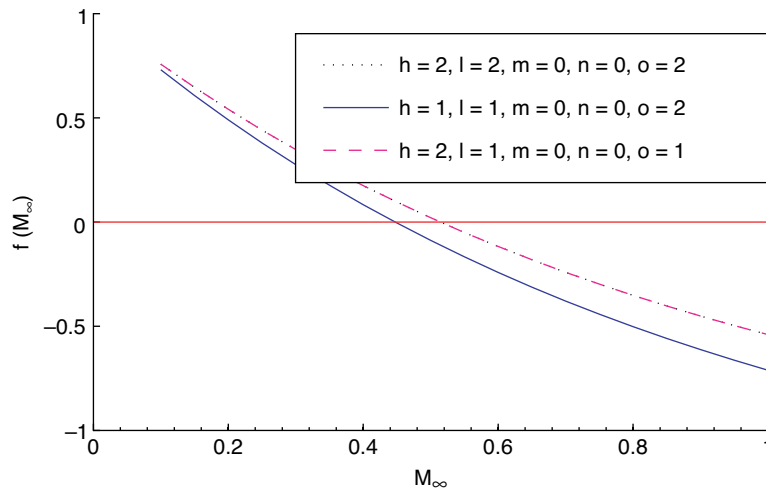


Figure 5. Normalized difference between the Strouhal number for longitudinal acoustic resonance and the Strouhal number of the first two Rossiter modes.

between the Strouhal number of the first Rossiter mode second harmonic $(h, o) = (1, 2)$ and that of the first longitudinal acoustic mode $(l, m, n) = (1, 0, 0)$. These two Strouhal number match at Mach 0.447, where the continuous blue curve crosses the abscissa. The dashed red curve shows the normalized difference between the Strouhal number of the second Rossiter mode $(h, o) = (2, 1)$ and that of the first longitudinal acoustic mode $(l, m, n) = (1, 0, 0)$. This curve overlaps the dotted black curve that shows the difference between the second Rossiter mode second harmonic $(h, o) = (2, 2)$ and the second longitudinal acoustic mode $(l, m, n) = (2, 0, 0)$. For these modes, their Strouhal numbers match at Mach 0.515.

The proximity of the Mach number investigated by Bissessur et al. [8] to Mach 0.515 indicates that acoustic resonance reinforcement may have affected the second Rossiter mode of the $L/D = 2$, $L/W = 1$ cavity at the selected inflow conditions.

4. MODELLING THE NATURAL ACOUSTIC MODES OF A CYLINDRICAL CAVITY

4.1. The Eigen-frequencies

In the cylindrical coordinates of figure 6, the Helmholtz equation, Eq. (3), becomes

$$\left(\frac{\partial^2}{\partial r^2} + \frac{1}{r} \frac{\partial}{\partial r} + \frac{1}{r^2} \frac{\partial^2}{\partial \theta^2} + \frac{\partial^2}{\partial z^2} + k_h^2 \right) p_h(r, \theta, z) = 0 \quad (27)$$

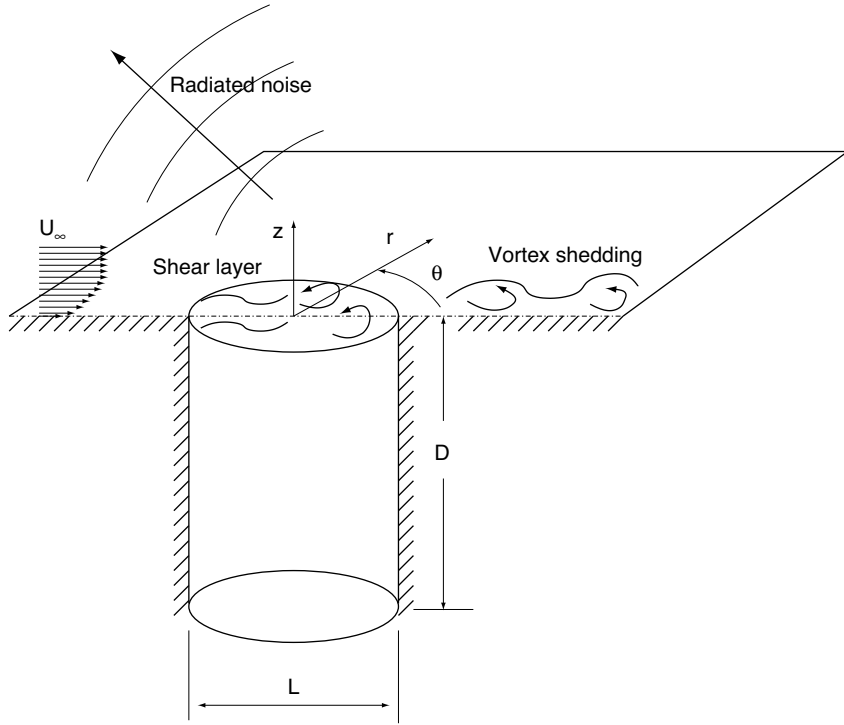


Figure 6. Cylindrical cavity geometry.

where subscript h indicates the h^{th} Fourier component of the time-dependent acoustic pressure fluctuation $p(r, \theta, z, t)$, as defined in Eq. (2). The boundary conditions of Eqs. (4) and (5) are re-cast in cylindrical coordinates as

$$p_h(r, \theta, z) = p_h(r, \theta + 2\pi, z) \quad (28)$$

$$p_h(0, \theta, z) \in \Re \quad (29)$$

$$\left(\frac{\partial}{\partial r} + \frac{1}{r} \right) p_h(R, \theta, z) = 0 \quad (30)$$

$$\frac{\partial}{\partial z} p_h(r, \theta, -D) = 0 \quad (31)$$

$$\frac{\partial}{\partial z} p_h(r, \theta, 0) = 0 \quad (32)$$

Whereas there is a straight-forward correspondence between Eq. (5) and Eq. (32), the relationship between Eq. (4) and Eqs. (28)-(31) is less immediate. Recall that, by virtue of the Helmholtz equation being a second-order partial differential equation, its integration requires exactly two independent boundary conditions per spatial dimension. As there is no solid boundary normal to θ in figure 6, Eq. (4) is always satisfied in the θ direction by virtue of the θ -normal boundaries having zero extent. Therefore two replacement boundary conditions are required in θ to integrate Eq. (27). These are obtained by imposing that the pressure field in θ matches itself with a periodicity of 2π , as stated in Eq. (28). It is worth noting that Eq. (28) constitutes two boundary conditions in θ , imposed respectively on the $\theta = 0$ lower θ boundary and on the $\theta = 2\pi$ upper θ boundary.

In the radial direction, it is imposed that the acoustic pressure fluctuation along the $r = 0$ axis is finite, which gives Eq. (29), and that the acoustic particle velocity normal to the cylindrical solid wall of diameter $L = 2R$ is zero, which is Eq. (4) applied on the cylindrical wall that gives Eq. (30). Finally, applying Eq. (4) on the cavity solid floor gives Eq. (31) that completes the set of boundary conditions for a cylindrical open cavity.

The solution of Eq. (27) with the boundary conditions of Eqs. (28)-(32) follows the same separation of variables approach as for the Helmholtz equation in Cartesian coordinates, detailed in Subsection 3.1. Let $p_h(r, \theta, z) = p_r(r) p_\theta(\theta) p_z(z)$, then Eq. (27) decouples into

$$\left(\frac{\partial^2}{\partial r^2} + \frac{1}{r} \frac{\partial}{\partial r} + k_h^2 - \frac{\eta^2}{r^2} - \zeta^2 \right) p_r = 0 \quad (33)$$

$$\left(\frac{\partial^2}{\partial \theta^2} + \eta^2 \right) p_\theta = 0 \quad (34)$$

$$\left(\frac{\partial^2}{\partial z^2} + \zeta^2 \right) p_z = 0 \quad (35)$$

where η and ζ are constants, independent from r , θ and z .

Equation (35) with the boundary conditions of Eqs. (31) and (32) is identical to its Cartesian counterpart, Eq. (17) with the boundary conditions of Eqs. (10) and (11). Therefore Eq. (18) with $l_z = D$ satisfies Eq. (35) and the boundary conditions of Eqs. (31) and (32).

Equation (34) has the same form of its Cartesian counterpart, Eq. (16), so its general solution is $p_\theta = A_\theta \cos(\eta\theta - \alpha_\eta)$. Substituting this in Eq. (28) gives $\eta = \pm m$, where $m \geq 0$ is an integer. Therefore

$$p_\theta = A_\theta \cos(\pm m\theta - \alpha_m) \quad (36)$$

where α_m is the phase-shift angle with respect to the $\theta = 0$ direction. α_m remains indeterminate, as there is no solid boundary nor other reference to lock any of the azimuthal modes to a specific phase angle in a cylindrical cavity with smooth walls. The numerical experiments by Grottadaurea & Rona [11,12] indicate that α_m tends to align normal to the azimuthal direction of the free-stream flow velocity above the cavity opening.

In Eq. (36), $\eta = +m$ and $\eta = -m$ satisfy independently the boundary conditions of Eq. (28), therefore the azimuthal acoustic pressure fluctuation can be made up of any arbitrary combination of anti-clockwise $+m$ modes and clockwise $-m$ modes of arbitrary amplitudes A_θ and B_θ and phase angles α_m and β_m . This allows to re-cast Eq. (36) as

$$p_\theta = A_\theta \cos(m\theta - \alpha_m) + B_\theta \cos(-m\theta - \beta_m) \quad (37)$$

Let $\xi^2 = k_h^2 - \zeta^2$. Substituting for ξ and for $\eta = \pm m$ in Eq. (33) gives

$$\left(\frac{\partial^2}{\partial r^2} + \frac{1}{r} \frac{\partial}{\partial r} + \xi^2 - \frac{m^2}{r^2} \right) p_r = 0 \quad (38)$$

The general solution to Eq. (38) is $p_r = A_r J_m(\xi r) + B_r Y_m(\xi r)$, where A_r and B_r are the amplitudes of the radial acoustic pressure fluctuation, independent from r , J_m is the m^{th} order Bessel function of the first kind and Y_m is the m^{th} order Bessel function of the second kind. As Y_m is singular at $r = 0$, by the boundary condition of Eq. (29), $B_r = 0$. Substituting $p_r = A_r J_m(\xi r)$ in Eq. (30) gives

$$\xi r \frac{\partial}{\partial \xi r} J_m(\xi R) + J_m(\xi R) = 0 \quad (39)$$

and using the Bessel function property $\xi r J'_m(\xi r) = m J_m(\xi r) - \xi r J_{m+1}(\xi r)$

$$\frac{J_m(\xi R)}{J_{m+1}(\xi R)} = \frac{\xi R}{m+1} \quad (40)$$

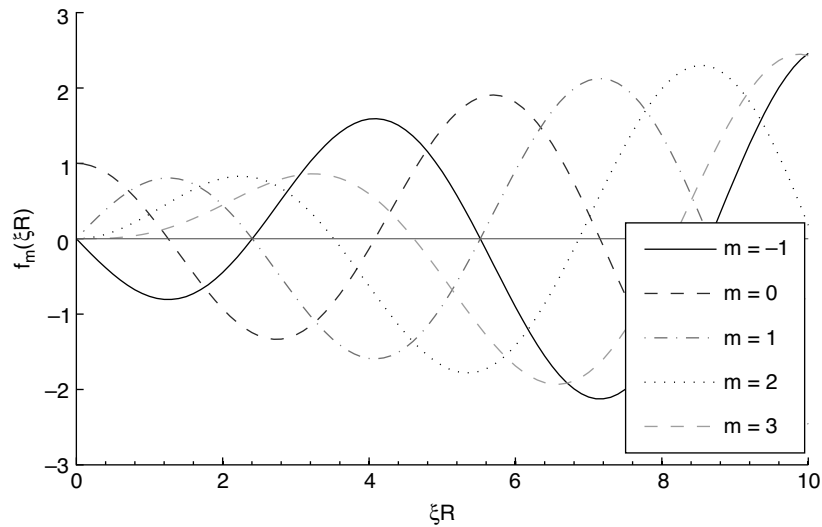


Figure 7. Eigenfrequency function.

Equation (40) can be solved numerically for ξ , to determine the wavenumbers that satisfy the radial component of the Helmholtz equation with a cylindrical rigid wall as boundary condition. Figure 7 shows $f_m(\xi R) = (m+1)J_m - \xi R J_{m+1}$ plotted over the range $0 \leq \xi R \leq 10$. f_m is evaluated for five values of m specifically, $m = 0$, representing the axisymmetric modes, $m = \pm 1$, representing the first clockwise and anti-clockwise azimuthal or spinning modes, and $m = 2$ and 3 , representing higher order anti-clockwise spinning modes. The intercepts of f_m with the abscissa are the roots of Eq. (40). Due to the Bessel function properties $J_m = (-1)^m J_{-m}$ and $2mJ_m = \xi R(J_{m+1} + J_{m-1})$, $f_m = (-1)^m f_{-m}$, which implies that clockwise and anti-clockwise spinning modes of the same order $|m|$ share the same eigen-value root of Eq. (40), therefore they have the same propagation characteristic. This enables an easy energy transfer between these mode pairs, so that, if a cylindrical cavity is forced at one spinning mode eigen-frequency, azimuthal waves may appear with a dominant clockwise or anti-clockwise component. When the clockwise and anti-clockwise mode pair have about the same modal amplitude, the instability will appear as an anti-symmetric fluctuation about the $\theta = \alpha_m + \pi/2$ axis. An anti-symmetric instability is predicted by a numerical cylindrical cavity model of Grottadaurea & Rona [11,12], although the frequency predicted by the numerical model is lower, indicating that the anti-symmetric instability is probably fluid-dynamic rather than due to resonant acoustic modes.

Table 1. Cylindrical cavity natural circular wavenumbers, $\xi_{l,m}R$.

m	0	± 1	2	3
$l = 0$	–	0	0	0
$l = 1$	1.2556	2.4048	3.5180	4.6123
$l = 2$	4.0793	5.5201	6.8661	8.1576

The oscillatory nature of the Bessel function is such that, for any given m , there is an infinite number of intersections of f_m with the abscissa over the range $\xi R \geq 0$. This gives three intersections or roots of Eq. (40) in the range $0 \leq \xi R \leq 10$ for $m = 0$ and similar multiple roots for $m \neq 0$. Table 1 lists the first three intersections along the ξR axis in the positive direction, starting from $\xi R = 0$. These have been numbered consecutively for increasing ξR , so that $\xi_{l,m}R$ is the l^{th} root of the azimuthal mode m , where $l \geq 0$ is integer. The radial acoustic pressure distribution is therefore given by

$$p_r = A_{l,m} J_m(\xi_{l,m} r) \quad (41)$$

The roots in table 1 were obtained by evaluating f_m over the range $0 \leq \xi R \leq 10$ at increments of $\Delta \xi R = 0.1$ and by interpolating linearly between each ξR pair lying on either side of each zero crossing. This technique was chosen in favour of a conventional Newton-Raphson iteration as the latter would have converged to just one out of the l possible roots of Eq. (40), for any given value of m . The root to which the method would have converged depends on the initial guess of $\xi_{l,m}R$ that is used to prime the root search. The oscillatory nature of the Bessel function is such that a poor initial guess for $\xi_{l,m}R$, for instance close to a maximum of f_m , would have resulted in the method finding a root remote from $\xi_{l,m}R$, due to the local shallow gradient of f_m . This may have led to some roots being missed out. The step by step searching of the roots prevented root skipping and produced results accurate to two decimal places. As f_m is monotonic over the interval ± 0.005 about each stated root, a Newton-Raphson iteration can make use of the values in table 1 as the starting point to reach an arbitrarily high level of significant digits.

From table 1 it can be noticed that the roots are interlaced, so that $\xi_{l,m}R < \xi_{l,m+1}R < \xi_{l+1,m}R$. This indicates that a higher azimuthal mode intercalates two consecutive radial modes in frequency. It is also of interest to note that the circular mode eigenvalues corresponding to a uniform radial pressure

distribution are $\xi_{l=0, |m| \geq 1} R$, so that they are degenerate spinning modes and not degenerate axisymmetric modes.

The $m = 0$ axisymmetric modes are shown in Subsection 4.3 to give rise to an acoustic particle velocity distribution that is singular at $r = 0$. This arises from the conservation of momentum of cylindrical waves collapsing on the axis of symmetry. Such a singularity is non-physical and would be prevented by the action of viscosity in a real fluid, which would dissipate the modal energy into heat. Therefore, the cylindrical cavity cannot support an undamped standing axisymmetric wave and the axisymmetric modes can only occur as damped modes in the system. The reader should be mindful of such a feature for the purpose of establishing the lowest self-sustained acoustic resonant eigenvalue of a cylindrical cavity.

From $\xi^2 = k_h^2 - \zeta^2$, $\omega_h = a_c k_h$ and $\omega_h = 2\pi f_h$, then the acoustic resonant eigenvalues for a cylindrical cavity are

$$f_{l,m,n} = \frac{a_c}{2\pi} \left[\xi_{l,m}^2 + \left(\frac{n\pi}{D} \right)^2 \right]^{1/2} \quad (42)$$

where l , m and n are integers ≥ 0 and $\xi_{l,m}$ is obtained from table 1 by dividing the stated values by the cylinder radius R .

4.2. The Eigenvectors

The acoustic pressure perturbation at any given acoustic resonance frequency $f_{l,m,n}$ inside a cylindrical cavity is obtained by combining Eqs. (18), (37) and (41) by $p_h(r, \theta, z) = p_r(r) p_\theta(\theta) p_z(z)$. This gives

$$p_{l,m,n}(r, \theta, z) = A_{l,m,n} J_m(\xi_{l,m} r) \cos(m\theta - \alpha_m) \cos(n\pi z/D) \\ + B_{l,m,n} J_m(\xi_{l,m} r) \cos(-m\theta - \beta_m) \cos(n\pi z/D) \quad (43)$$

Given that $J_{-m} = (-1)^m J_m$, by factorizing $(-1)^m$ out of the mode amplitude $B_{l,m,n}$, Eq. (43) can be re-cast as

$$p_{l,m,n}(r, \theta, z) = A_{l,m,n} J_m(\xi_{l,m} r) \cos(m\theta - \alpha_m) \cos(n\pi z/D) \quad (44)$$

where $0 \leq l < \infty$, $-\infty < m < \infty$ and $0 \leq n < \infty$ are arbitrary integers.

Figures 8 and 9 show the first six acoustic resonant spinning modes of a cylindrical cavity of diameter to depth ratio $L/D = 0.714$. This is the geometry investigated numerically by Grottadaurea & Rona [11,12]. The natural modes are shown of unit amplitude on the $z = -D/2$ plane, lengths are normalized by

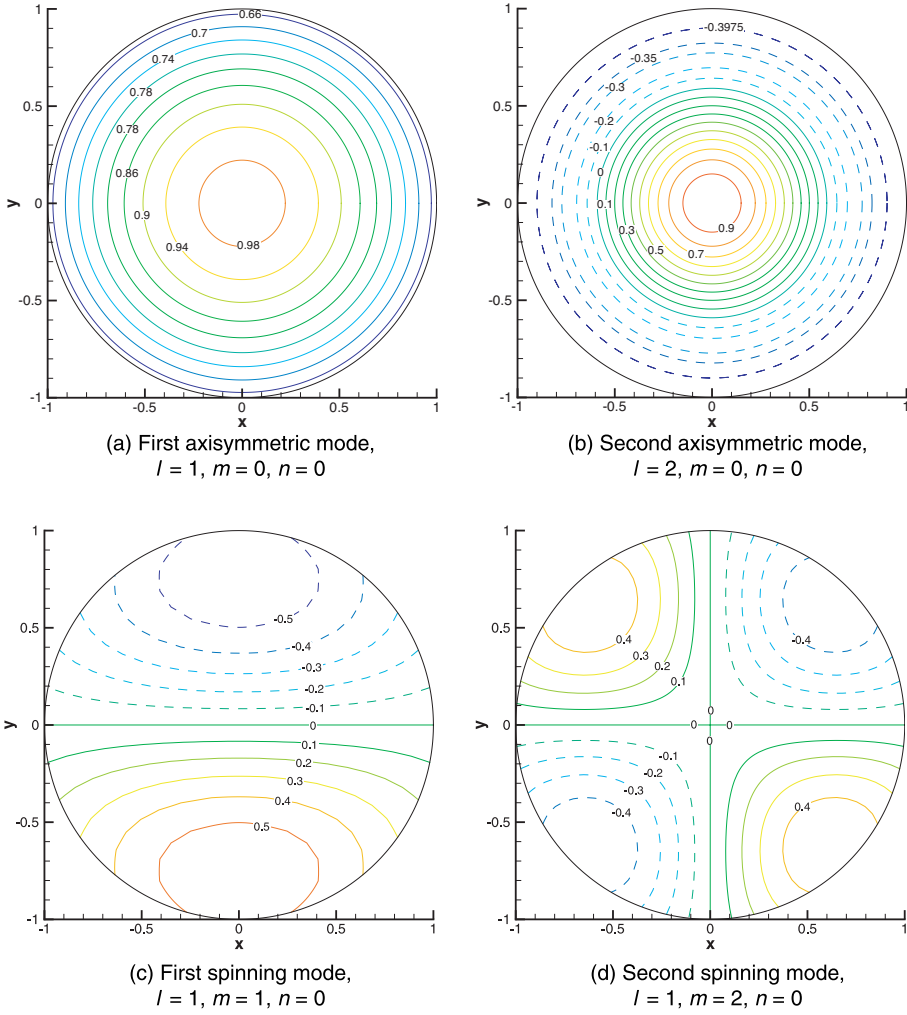


Figure 8. Pressure eigenmodes in a cylinder with rigid walls.

the cavity diameter L and the phase reference angle $\alpha_m = \pi/2$ for all m . There is some similarity between the second spinning mode $(l, m, n) = (1, 2, 0)$ and the anti-symmetric shear-layer pattern predicted by Grottadaurea & Rona [11,12] across the cavity opening.

The time-dependent acoustic pressure fluctuation inside the cylindrical cavity due to the resonant modes can be reconstructed by a linear summation of the contributions from all modes, according to Eq. (2). As the cylindrical eigenvectors are orthogonal, then

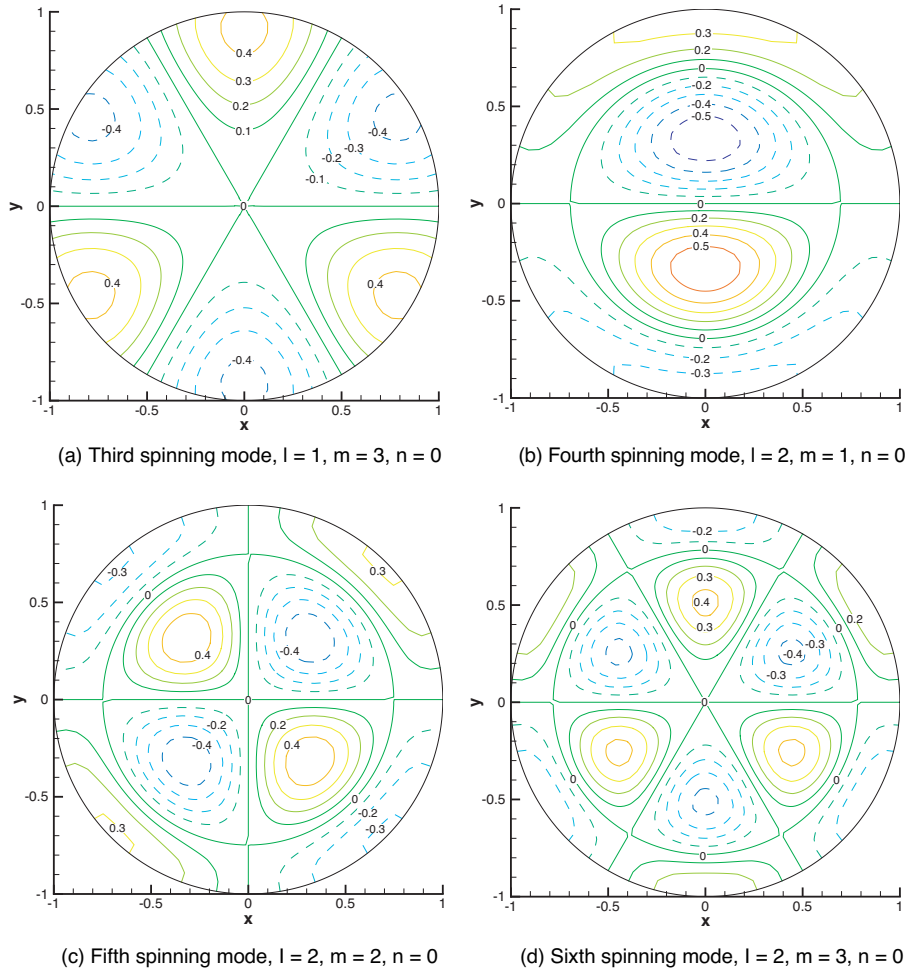


Figure 9. Pressure eigenmodes in a cylinder with rigid walls.

$$p(r, \theta, z, t) = \sum_{l=0}^{\infty} \sum_{m=-\infty}^{\infty} \sum_{n=0}^{\infty} p_{l,m,n}(r, \theta, z) \cos(2\pi f_{l,m,n}t - \phi_{l,m,n}) \quad (45)$$

where $\phi_{l,m,n}$ is the phase angle of mode (l, m, n) at time $t = 0$.

4.3. The Acoustic Velocity Inside a Cylindrical Cavity

The acoustic velocity vector $\mathbf{u}(\mathbf{x}, t)$ induced by the acoustic pressure field of Eq. (45) can be estimated by applying Newton's second law to an elemental inviscid fluid particle of volume V bounded by a closed surface \mathbf{S} . The net pressure force acting on \mathbf{S} is equal to the particle mass times its acceleration. Therefore

$$\int_V \rho \frac{\partial \mathbf{u}(\mathbf{x}, t)}{\partial t} dV = \oint_s p(\mathbf{x}, t) \mathbf{n} dS \quad (46)$$

where \oint_s is a clockwise surface integral. By taking the surface integral anti-clockwise and applying the Gauss divergence theorem, Eq. (46) becomes

$$\int_V \rho \frac{\partial \mathbf{u}(\mathbf{x}, t)}{\partial t} dV = -\oint_s p(\mathbf{x}, t) \mathbf{n} dS = -\int_V \nabla p(\mathbf{x}, t) \cdot \mathbf{n} dV \quad (47)$$

In the limit of the particle volume being vanishingly small, which is $\lim V \rightarrow 0$, then $\rho \partial \mathbf{u}(\mathbf{x}, t) / \partial t = -\nabla p(\mathbf{x}, t)$. Integrating with respect to time gives

$$\mathbf{u}(\mathbf{x}, t) = -\int_0^t \frac{1}{\rho} \nabla p(\mathbf{x}, t) dt \quad (48)$$

Substituting Eq. (45) in Eq. (48) gives the acoustic velocity distribution inside a cylindrical cavity, which is

$$\mathbf{u}(r, \theta, z, t) = \sum_{l=0}^{\infty} \sum_{m=-\infty}^{\infty} \sum_{n=0}^{\infty} \mathbf{u}_{l,m,n}(r, \theta, z) \left[\cos\left(\omega_{l,m,n}t - \phi_{l,m,n} + \frac{\pi}{2}\right) - \sin \phi_{l,m,n} \right] \quad (49)$$

$$\mathbf{u}_{l,m,n}(r, \theta, z) = \frac{\nabla p_{l,m,n}(r, \theta, z)}{\rho_c \omega_{l,m,n}} \quad (50)$$

where $\omega_{l,m,n} = 2\pi f_{l,m,n}$ is the circular frequency of mode (l, m, n) . In performing the integration of Eq. (48), the integrand has been linearized with respect to the density ρ_c of the unperturbed flow inside the cavity. This linearization derives from the same isentropic perturbation assumption of Eq. (1), by which the acoustic density perturbations $\ll \rho_c$. Equation (50) states that the spatial distribution of the acoustic velocity of any acoustic natural mode (l, m, n) is obtained from the gradient of the acoustic mode pressure. Let $\mathbf{u}_{l,m,n}(r, \theta, z) = (u_r, u_\theta, u_z)$, then substituting Eq. (44) into Eq. (50) the radial, azimuthal and axial components of the acoustic velocity for mode (l, m, n) are

$$\begin{aligned} u_r &= \frac{1}{\rho_c \omega_{l,m,n}} \left(\frac{\partial}{\partial r} + \frac{1}{r} \right) [A_{l,m,n} J_m(\xi_{l,m} r) \cos(m\theta - \alpha_m) \cos(n\pi z / D)] \\ &= \frac{A_{l,m,n}}{\rho_c \omega_{l,m,n}} \frac{\xi_{l,m}}{2m} [(m+1)J_{m-1}(\xi_{l,m} r) - (m-1)J_{m+1}(\xi_{l,m} r)] \\ &\quad \times \cos(m\theta - \alpha_m) \cos(n\pi z / D) \end{aligned} \quad (51)$$

$$\begin{aligned}
u_\theta &= \frac{1}{\rho_c \omega_{l,m,n}} \frac{\partial}{r \partial \theta} [A_{l,m,n} J_m(\xi_{l,m} r) \cos(m\theta - \alpha_m) \cos(n\pi z / D)] \\
&= -\frac{A_{l,m,n}}{\rho_c \omega_{l,m,n}} \frac{\xi_{l,m}}{2} [J_{m+1}(\xi_{l,m} r) + J_{m-1}(\xi_{l,m} r)] \\
&\quad \times \sin(m\theta - \alpha_m) \cos(n\pi z / D)
\end{aligned} \tag{52}$$

$$\begin{aligned}
u_z &= \frac{1}{\rho_c \omega_{l,m,n}} \frac{\partial}{\partial z} [A_{l,m,n} J_m(\xi_{l,m} r) \cos(m\theta - \alpha_m) \cos(n\pi z / D)] \\
&= -\frac{n\pi}{D} \frac{A_{l,m,n}}{\rho_c \omega_{l,m,n}} J_m(\xi_{l,m} r) \cos(m\theta - \alpha_m) \sin\left(\frac{n}{D} \pi z\right)
\end{aligned} \tag{53}$$

Equation (51) is valid $\forall m \neq 0$. For $m = 0$, Eq. (51) can be re-cast as

$$u_r = \frac{A_{l,0,n}}{\rho_c \omega_{l,0,n}} \xi_{l,0} \left(\frac{J_0(\xi_{l,0} r)}{\xi_{l,0} r} - J_1(\xi_{l,0} r) \right) \tag{54}$$

Equation (54) is singular on the cylinder axis $r = 0$, which derives from the conservation of momentum of a cylindrical wave collapsing on the cylindrical cavity axis. In a real viscous flow, the acoustic velocity fluctuation on the axis will be finite, resulting in damped axisymmetric modes. Figures 10(a) and 10(b) show the acoustic velocity distribution for the first two axisymmetric modes. Figure 10(a) shows a monotonic increment of the acoustic velocity from the cylindrical wall towards the centre, as indicated by the concentric velocity iso-contour lines. The velocity distribution in a small region around the cylinder axis where the velocity becomes singular has been excluded from the plot. In Fig. 10(b), the monotonic increase of acoustic velocity towards the cylinder axis starts from a nodal plane of radius $\sim 0.25R$, resulting in a sharper rise in acoustic velocity towards the cylinder axis and in a smaller region where the large amplitude velocity fluctuations in a real fluid will be significantly damped by viscosity.

Figures 10(c) and 10(d) show a vector plot of the acoustic velocity distribution of the first two azimuthal modes. The velocity magnitude at each position inside the cylindrical walls is shown normalized by the mode amplitude $A_{l,m,n}/(\rho a_c)$. For convenience, the velocity magnitude distribution is shown both by the variations in the vector length and colour. The reference unit vector and the colour scale are given to the right of each figure. Around the cylindrical walls, the velocity is shown as tangential to the surface, confirming the successful

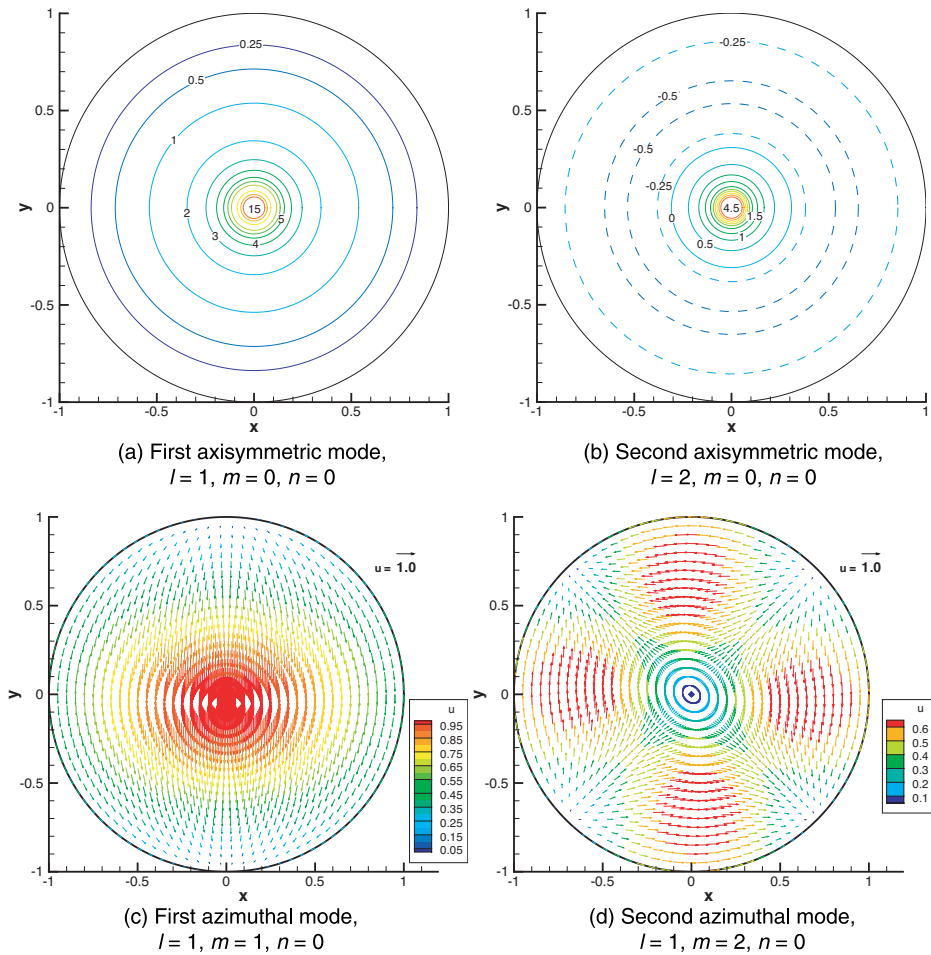


Figure 10. Acoustic velocity in a cylinder with rigid walls.

implementation of the inviscid solid wall boundary condition of Eq. (30). The acoustic velocity of Fig. 10(c) is driven by two acoustic pressure anti-nodes at either side of the $\theta = 0$ diameter, shown in Fig. 8(c). This induces an acoustic velocity maximum in the $\theta = 3\pi/2$ direction at the mid-point between the two pressure anti-nodes. The acoustic velocity is minimum at the pressure anti-node locations. In Fig. 10(d), four pressure antinodes in Fig. 8(d) located at $\theta = \pm\pi/4$ and $\theta = \pm3\pi/4$ drive four velocity maxima at mid-points between the anti-nodes, at $\theta = 0$, $\theta = \pi$, and $\theta = \pm\pi/2$. Four velocity minima are at the anti-node locations. The same pattern of velocity maxima intercalating pressure anti-nodes repeats for the higher azimuthal mode numbers in Fig. 11.

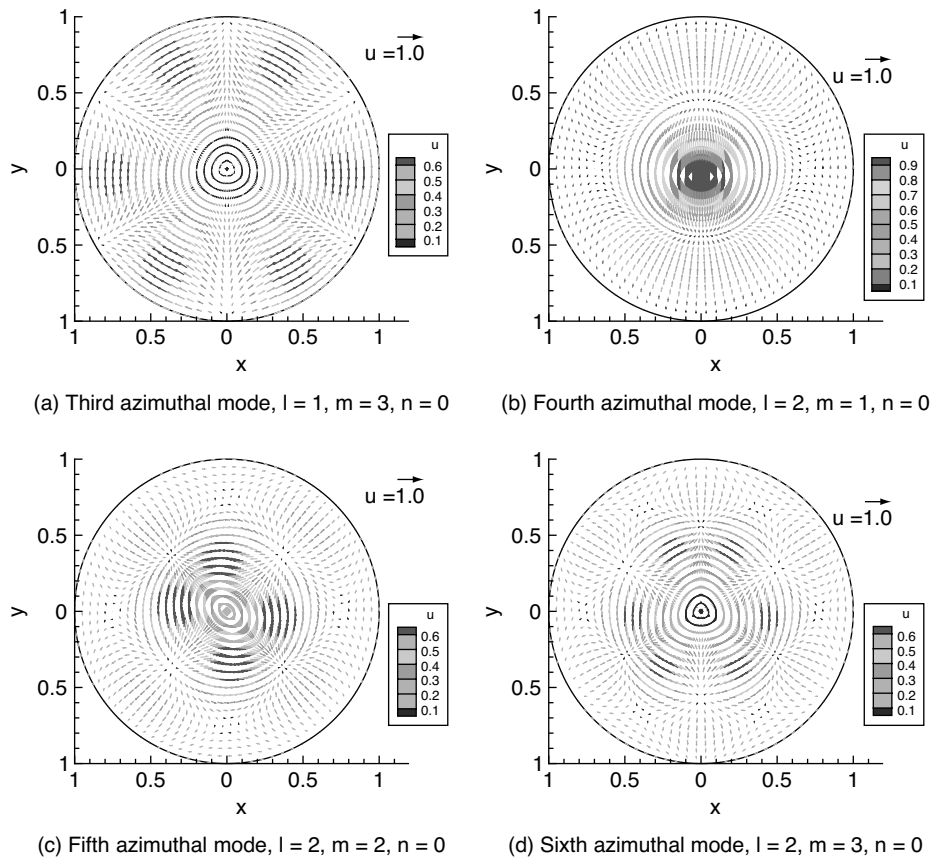


Figure 11. Acoustic velocity in a cylinder with rigid walls.

4.4. Cylindrical Cavity Instability Reinforcement by Acoustic Resonance

Equation (42) can be used to determine whether, for a given cylindrical cavity diameter to depth ratio, a fluid dynamic instability is likely to be reinforced by acoustic resonance. Let L be the cavity diameter and U_∞ the free-stream velocity of a flow blowing tangentially over the cavity opening. The cylindrical cavity acoustic natural frequencies can be re-stated as Strouhal numbers

$$Str_{l,m,n} = \frac{f_{l,m,n} L}{U_\infty} = \frac{\left(1 + \frac{\gamma-1}{2} M_\infty^2\right)^{1/2}}{M_\infty} \left[\left(\frac{\xi_{l,m} R}{\pi} \right)^2 + \left(\frac{n L}{2 D} \right)^2 \right]^{1/2} \quad (55)$$

Figure 12 shows the predicted acoustic Strouhal numbers from Eq. (55) for $L/D = 0.714$. These predictions were obtained by coding Eq. (55) in Matlab

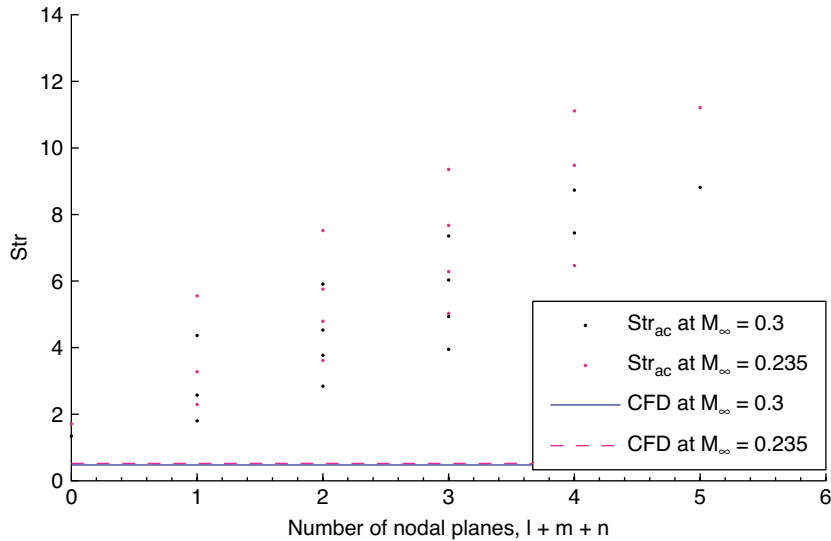


Figure 12. Fluid dynamic and acoustic Strouhal numbers of a $L/D = 0.714$, cylindrical cavity. Acoustic Strouhal numbers at Mach 0.235 (·) and at Mach 0.3 (·), CFD predictions [11,12] at Mach 0.235 (---) and at Mach 0.3 (—).

7.0.4 and the script was run on a desktop computer with a 3GHz Intel Pentium 4 processor and 1GB of RAM. The predictions at a free stream Mach number $M_\infty = 0.235$ are shown by the red dots and at $M_\infty = 0.3$ are shown by the black dots. The Strouhal numbers of the first 15 modes are shown at each Mach number condition. These are plotted against the number of nodal planes in the corresponding eigenvectors, or mode shapes, which is a measure of the mode shape complexity. Numerical predictions of the cylindrical cavity flow were obtained on a node of $4 \times 2.2\text{GHz}$ AMD Opteron 848 Processors with 8GB RAM [11,12]. At $M_\infty = 0.235$, these indicate that the cavity exhibits a fluid dynamic self-sustained instability at a Strouhal number $Str = 0.5295$. This Strouhal number is marked by the red dashed line in Fig. 12. At $M_\infty = 0.3$, the fluid dynamic instability Strouhal number is predicted [11,12] to be $Str = 0.491$ and it is marked by the continuous black line in Fig. 12. The acoustic and fluid dynamic Strouhal numbers for a nodal plane number of 0 and 1 are significantly different, indicating that the two instability mechanisms are not interacting at the selected flow conditions. The acoustic Strouhal numbers increase with the number of nodal planes, therefore preventing any significant acoustic-fluid dynamic resonance that involve higher acoustic mode numbers.

Figure 13 shows the acoustic Strouhal numbers computed at the same inflow conditions for a $L/D = 2.5$ cavity. The red dots mark the acoustic Strouhal

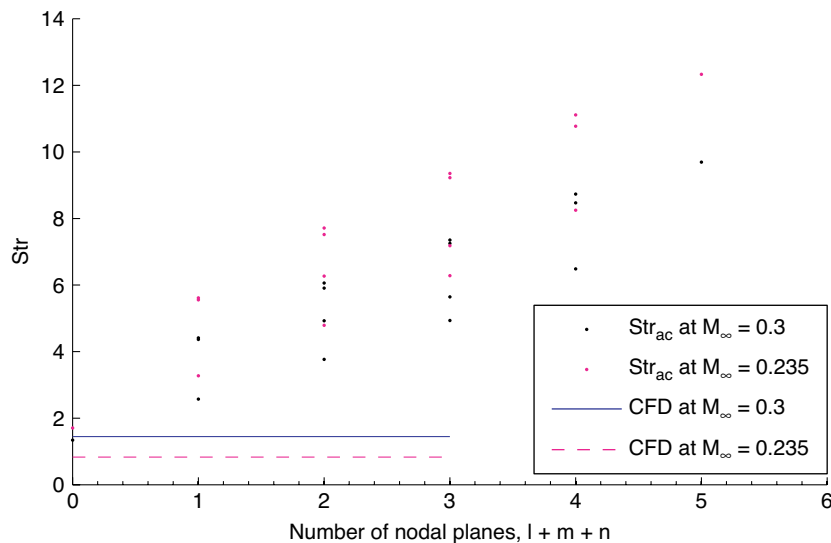


Figure 13. Fluid dynamic and acoustic Strouhal numbers of a $L/D = 2.5$, cylindrical cavity. Acoustic Strouhal numbers at Mach 0.235 (\cdot) and at Mach 0.3 (\cdot), CFD predictions [11,12] at Mach 0.235 (—) and at Mach 0.3 (—).

numbers predicted at Mach 0.235 and the black dots show the acoustic Strouhal numbers at Mach 0.3. At the free-stream Mach numbers of 0.235 and 0.3, a $L/D = 2.5$ cylindrical cavity exhibits a fluid dynamic instability at $Str = 0.833$ and $Str = 1.448$, respectively [11,12]. These fluid dynamic Strouhal numbers are marked by the discontinuous red line and continuous black line in Fig. 13. The acoustic azimuthal mode Strouhal numbers closest to the fluid dynamic ones are $Str = 3.27$ at Mach 0.235 and $Str = 2.57$ at Mach 0.3. These are sufficiently far from the fluid dynamic Strouhal numbers so that coupling between these modes is unlikely at the selected test conditions. The first acoustic axisymmetric mode, that has a number of nodal planes equal to zero, has instead a Strouhal number that is close to the fluid dynamic one at Mach 0.3. However, as this acoustic mode is damped, it is unlikely generate an amplification of the fluid dynamic resonance.

5. CONCLUSION

An analytical method is presented to estimate the acoustic resonant modes of an open cavity, which is applicable to an arbitrary shaped enclosure. The method is applied to determine the acoustic resonant eigen-frequencies and mode shapes of a rectangular and of a cylindrical cavity.

The model is of practical use to determine whether acoustic resonance can reinforce fluid dynamic instabilities that often characterize open cavity flows. As a practical example, the interaction between the acoustic resonance and the Rossiter modes in an $L/D = 2$, $L/W = 1$, Mach 0.6 model cavity flow was considered. It was found that, at the selected test conditions, the coupling between the fluid dynamic and acoustic instabilities was likely for the Rossiter 2 mode and its second harmonic.

The application of the analytical method to a cylindrical geometry highlighted salient physical aspect of acoustic resonance in a cylinder with rigid walls. It was determined that an axisymmetric standing wave pattern cannot be realized in a real flow, due to the high acoustic particle velocity that occurs at the cylinder axis. The absence of a geometrical reference point in the azimuthal direction around smooth cavity walls leaves the zero phase angle of azimuthal modes indeterminate. In practice, this means that azimuthal cavity resonant modes may precess over time. Therefore, a control strategy for such a flow resonant instability may start by considering the addition of a tab around the walls to act as a phase reference lock for the azimuthal modes, so to reduce the degrees of freedom the controller has to tackle. Also, when experiments are conducted on a cylindrical cavity flow, attention must be paid to any azimuthal precession of any nodal plane of the flow instabilities during the test, for instance, by including an adequate monitoring strategy of the pressure phase around the cylinder perimeter.

The analytical method was used to check for any frequency coupling between the aerodynamic instability of a cylindrical cavity with aspect ratios 0.714 and 2.5 tested at Mach numbers 0.235 and 0.3 and the acoustic modes of the cylinder. No evidence of such coupling was found over the range of acoustic mode numbers tested.

ACKNOWLEDGEMENT

This research project has been supported by a Marie Curie Early Stage Research Training Fellowship of the European Community's Sixth Framework Programme under contract number MEST CT 2005 020301. The help of Marco Cambiano in the initial stage of the research is acknowledged.

REFERENCES

- [1] A. Charwat, J. Roos, F. Dewey, J. Hitz, An investigation of separated flows. Part I: The pressure field, *J. Aerospace Sci.* 28 (6) (1961) 457–470.

- [2] C. Rowley, D. Williams, Dynamics and control of high-Reynolds-number flow over open cavities, *Annual Review of Fluid Mechanics* 38 (2006) 251–276.
- [3] V. Theofilis, Advances in global linear instability analysis of nonparallel and three-dimensional flows, *Progress in Aerospace Sciences* 39 (2003) 249–315.
- [4] E. Covert, An approximate calculation of the onset velocity of cavity oscillations, *Journal of the American Institute of Aeronautics and Astronautics* 8 (12) (1970) 2189–2194.
- [5] J. C. Hardin, D. S. Pope, An acoustic/viscous splitting technique for computational aeroacoustics, *Theoretical and computational fluid dynamics* 6 (5-6) (1994) 323–340.
- [6] S. Slimon, D. Davis, C. Wagner, Far-field aeroacoustic computation of unsteady cavity flows, Conference Paper 98-0285, AIAA, 36th Aerospace Sciences Meeting and Exhibit, 12-15 January 1998, Reno, NV, USA (1998).
- [7] Z.-K. Wang, G. S. Djambazov, C.-H. Lai, K. A. Pericleous, Numerical investigation of a source extraction technique based on an acoustic correction method, *Computers and Mathematics with Applications* doi:10. 1016/j.camwa.2004.08.017, to appear.
- [8] R. Bissessur, X. Chen, X. Zhang, Numerical investigation of subsonic 2D/3D cavity flows, Conference Paper 2004-0683, AIAA, 42nd AIAA Aerospace Sciences Meeting and Exhibit, 5-8 January 2004, Reno, NV (2004).
- [9] H. Heller, D. Bliss, The physical mechanism of flow-induced pressure fluctuations in cavities and concepts for their suppression, Conference Paper 1975-491, 2nd AIAA Aeroacoustics Conference, 24-26 March 1975, Hampton, VA, USA (1975).
- [10] C. Tam, P. Block, On the tones and pressure oscillations induced by flow over rectangular cavities, *J. Fluid Mechanics* 89 (1978) 373–399.
- [11] M. Grottadaurea, A. Rona, Noise sources from a cylindrical cavity, Conference Paper 2007-3723, AIAA, 13th AIAA/CEAS Aeroacoustics Conference, 21-23 May 2007, Rome, Italy (2007).
- [12] M. Grottadaurea, A. Rona, The role of the inflow momentum thickness in subsonic cylindrical cavity noise generation, Conference Paper 165, IIAV, 14th International Congress on Sound and Vibration, 9-12 July 2007, Cairns, Australia (2007).

